



HAL
open science

Effects of Size and Morphology on the Excited State Properties of Nanoscale WO₃ Materials from First-Principles Calculations: Implications for Optoelectronics Devices

Valentin Diez-Cabanes, Alekos Segalina, Mariachiara Pastore

► **To cite this version:**

Valentin Diez-Cabanes, Alekos Segalina, Mariachiara Pastore. Effects of Size and Morphology on the Excited State Properties of Nanoscale WO₃ Materials from First-Principles Calculations: Implications for Optoelectronics Devices. ACS Applied Nano Materials, In press, 5 (11), pp.16289-16297. 10.1021/acsanm.2c03331 . hal-03871093

HAL Id: hal-03871093

<https://hal.science/hal-03871093>

Submitted on 25 Nov 2022

HAL is a multi-disciplinary open access archive for the deposit and dissemination of scientific research documents, whether they are published or not. The documents may come from teaching and research institutions in France or abroad, or from public or private research centers.

L'archive ouverte pluridisciplinaire **HAL**, est destinée au dépôt et à la diffusion de documents scientifiques de niveau recherche, publiés ou non, émanant des établissements d'enseignement et de recherche français ou étrangers, des laboratoires publics ou privés.



Distributed under a Creative Commons Attribution 4.0 International License

Effects of Size and Morphology on the Excited State Properties of Nanoscale WO₃ Materials from First-Principles Calculations: Implications for Optoelectronics Devices

Valentin Diez-Cabanes,^{1,} Alekos Segalina,^{1,2} Mariachiara Pastore^{1,*}*

¹ Université de Lorraine & CNRS, Laboratoire de Physique et Chimie Théoriques (LPCT), F-54000, Nancy, France

² Department of Chemistry, Korea Advanced Institute of Science and Technology (KAIST), 291 Daehak-ro, Yuseong-gu, Daejeon, 34141 Republic of Korea

*Authors to whom correspondence should be addressed: valentin.diez-cabanes@univ-lorraine.fr; mariachiara.pastore@univ-lorraine.fr

KEYWORDS Tungsten oxide nanostructures, absorption/emission properties, multiscale modelling, Time-Dependent Density Functional Theory, Bethe Salpeter Equation

ABSTRACT

Nowadays, the interest in tungsten oxide (WO₃) nanomaterials for many light-driven technologies is significantly increasing due to their good biocompatibility, strong light absorption, and stabilized emission at room temperature. However, the poor understanding achieved on the

photophysics of WO_3 nanostructures, when compared to other prototypical nanomaterials, such as TiO_2 , has largely mitigated their potential application as photo-active components in opto-electronic devices. In this context, we have developed a multi-scale modelling approach to shed light on the excited state properties (absorption and emission) of realistic WO_3 nanoparticles by means of Time-Dependent Density Functional Theory (TD-DFT) based methods. Upon validating our methodology against high-accurate perturbative methods and the available experimental data, we have demonstrated that the absorption and excitonic properties of the WO_3 NPs can be easily tuned by controlling their size and shape. In a second step, our calculations pointed to the use of small NPs with a high density of surface atoms (i.e. spherical NPs) as the best strategy to enhance the emission properties of these nanoparticles, demonstrating the importance of a judicious morphological design to improve the targeted opto-electronic properties in nanomaterials, thus opening the door to the practical exploitation of these materials in the field of opto-electronics.

1. Introduction

Nowadays, tungsten trioxide (WO_3) is one of the most employed materials for semiconductor technologies such as photocatalysis,¹ electrochromic devices,² phototherapy,³ sensors,⁴ and opto-electronics,⁵ due to its strong light absorption, easy processability, good biocompatibility, high stability in strong chemical environments, and photochromic behaviour.⁶ Most of these technologies employ nanostructured WO_3 materials as photoactive semiconductor due to several advantages when compared with their bulk phase.^{7,8} For instance, facet engineering the bulk structure can open the possibility to tune at choice the opto-electronic properties of the nanomaterial by carefully modifying their size and morphology.^{9,10} Furthermore, when reducing

the lateral dimensions of the nanostructure below a certain quantity (the Bohr radius), quantum confinement effects can assist the formation of stable electron-hole (e-h) pairs, yielding enhanced emission at room temperature, thus making low dimensional WO_3 materials very attractive for light-emitting or imaging devices.⁵ Nonetheless, despite overcoming some of the toxicity and stability issues exhibited by some traditional quantum dot (QD) materials,¹¹ up to now the practical application of WO_3 nanomaterials for opto-electronic applications (i.e. photodetectors, light emitters, memories) has been mainly limited by a lack of fundamental knowledge of their photophysical properties. Indeed, only a few examples of opto-electronic characterization of WO_3 QDs have been reported to date. Some works have been dedicated to the study of the band gap expansion in WO_3 QDs due to quantum confinement effects,¹² and their implications in the photocatalytic performance.^{13,14} These results evidenced that WO_3 nanomaterials are particularly sensitive to quantum confinement effects since the energy gaps (E_g) of the bulk phase can be increased by 1.1 eV via the reduction of the QD diameter up to 0.8 nm.¹² As a consequence, the absorption features of WO_3 NPs can be modified from a discrete band centered at 220-250 nm^{15,16} to a sharp continuous absorption with a band edge at 475 nm,^{17,18} by increasing the size of the nanoparticle (NP). Regarding their emission properties, despite no photoluminescence (PL) has been reported for the bulk WO_3 , as pointed out above, size confinement stabilizes the emission of low dimensional materials at room temperature, making it possible to observe broad PL emission peaks centered at 325-350 nm and 420-440 nm in the case of thin films,^{19,20} nanorods,²¹ and nanowires.²² Indeed, in the case of thin films, the PL peak energy can be monitored by varying their thickness.²³ Moreover, the modification of the morphology of the WO_3 nanomaterial enabled to shift their emission up to 470-475 nm in nanowire-like structures.^{24,25} In the case of WO_3 QDs, these materials displayed emission lines with different characteristics depending on their size: (i)

S. Cong et al. reported a sharp emission peak at $\lambda_{em}=300$ nm for 1.6 nm QDs upon excitation at $\lambda_{abs}=220$ nm,¹⁵ (ii) H. Peng et al. observed similar sharp emission of 1.3 nm QDs at $\lambda_{em}=400$ nm after excitation at $\lambda_{abs}=254$ nm,¹⁶ and (iii) S. Wang et al. detected a broader emission centered at $\lambda_{em}=461$ nm for 2.5 nm diameter QDs after excitation $\lambda_{abs}=348$ nm.²⁶ We can thus observe a reduction of the Stoke shifts from 1.8-1.5 eV to 0.9 eV when increasing the diameter of the QD from ~ 1.5 nm to 2.5 nm. Furthermore, the dependency of the emission peak with respect to the excitation wavelength is more pronounced in the case of the larger nanostructures,¹⁹ since the smallest QDs showed an emission band position which is independent of the excitation energy.^{15,16} However, the origin of this emission remains still unclear and different phenomena such as band-to-band recombination or the presence of defects (i.e. oxygen vacancies) are often invoked to this purpose. An additional factor affecting the optical absorption features of WO_3 nanomaterials is the morphology, as it was evidenced by J. Liao et al, demonstrating that the absorption edge of these materials can be finely tuned in a range of 2.3-2.9 eV by modifying the shape of the NP (nanoplates, rectangular nanosheet, microspheres or hexagonal nanowires and bundles).²⁷ We can thus conclude that the rationalization of the role played by quantum confinement and morphological effects in the absorption and emission properties of WO_3 nanostructures will definitively help toward their technological exploitation.

To this end, theory has been proved to be a valuable tool to shed light on the photophysical phenomena underlying the charge generation and recombination processes in semiconductor NPs, once realistic structural models and a reliable methodology are finely set up.^{28,29} In a previous work, we developed a combined GW^{30} - Density Functional Theory (DFT) protocol to get an estimation of the energetic levels of realistic WO_3 NPs within a GW level of accuracy.³¹ We

employed this methodology to draw important design rules to tune the energetic alignment in single WO_3 NPs³¹ and in WO_3/WO_3 and WO_3/TiO_2 NP heterojunctions,³² based on the morphological engineering of the NP structures. Nonetheless, these calculations were limited to the electronic structure of the WO_3 NPs in their ground state (GS), whereas for getting a complete picture of the photophysics of these systems one would need to perform excited states calculations within a reasonable level of accuracy. Generally, the methodologies used to this purpose in the case of medium and large systems are based on Time-dependent DFT (TD-DFT), which, however, usually require preliminary benchmark against experiments, showing generally a marked functional- and system-dependence.^{33,34} During the last years, however, many-body perturbation theory (MBPT) methods based on the resolution of the Bethe-Salpeter Equation (BSE) have become extremely popular due to their ability to provide a highly accurate and unbiased estimation of the excited state properties of small systems, making them especially suitable for benchmarking purposes.^{35,36} Unfortunately, both methods (TD-DFT and BSE) become computationally prohibitive for affording the excited state properties of realistic nanoscale systems owing thousands of atoms. In this regard, Grimme and co-workers developed an effective approach to decrease the computational cost of the linear optical response calculations by applying a series of approximations to solve the two-electron repulsion integrals, representing the major computational bottleneck for this type of calculations, meanwhile maintaining the essential physics of TD-DFT. This method, known as simplified TD-DFT (sTD-DFT or sTDA),^{37,38} provided results of comparable level of accuracy of TD-DFT, but within a much lower computational burden.³⁹

In this work, by employing the state-of-the-art methodologies mentioned above, we present a multi-scale modelling approach aimed at evaluating the influence of quantum confinement and

surface termination effects on the optical response of nanostructured WO_3 materials, by considering an extended set of realistic NPs of different sizes and morphologies. In a first step, we make use of the excited state properties estimated at the GW/BSE and the TD-DFT levels of theory to benchmark the results provided by sTD-DFT methods for small and medium size NPs, respectively. Afterwards, we employ this method (sTD-DFT) to provide a reliable structure-property relationship of the absorption features and exciton lifetimes of the WO_3 NPs by contrasting these results with the available experimental data. Finally, we employ the smallest NP models to rationalize the emission properties experimentally observed in WO_3 QDs. Our results demonstrate that sTD-DFT is able to reproduce the absorption properties of the NPs by including relatively large fractions of Hartree-Fock exchange, and that dimensional confinement and the NP morphologies are the key factors driving the optical properties of WO_3 QDs, what has allowed us to set up useful design rules to boost their absorption/emission characteristics based on morphological engineering their structure.

2. Theoretical Methodology

Nanostructure models

The NP structures considered in this study are the ones reported in our previous work,³¹ as they are represented in Figure 1. This set of NPs comprises $n=8, 27, 64, 125, 216,$ and 343 cubic $(\text{WO}_3)_n$ particles; rectangular-shaped $(\text{WO}_3)_n$ particles with $n=32, 147,$ and 400 ; spherical-shaped $(\text{WO}_3)_n$ particles with $n=19, 32, 80, 147$ and 281 ; hexagonal nanosheet $(\text{WO}_3)_n$ particles with $n=12, 24, 84, 144, 180$ and 420 ; cuboid nanowires $(\text{WO}_3)_n$ particles with $n=18, 24, 30, 36, 66, 126, 186$ and 306 . More details about the construction of the structures are given in the reference article.³¹

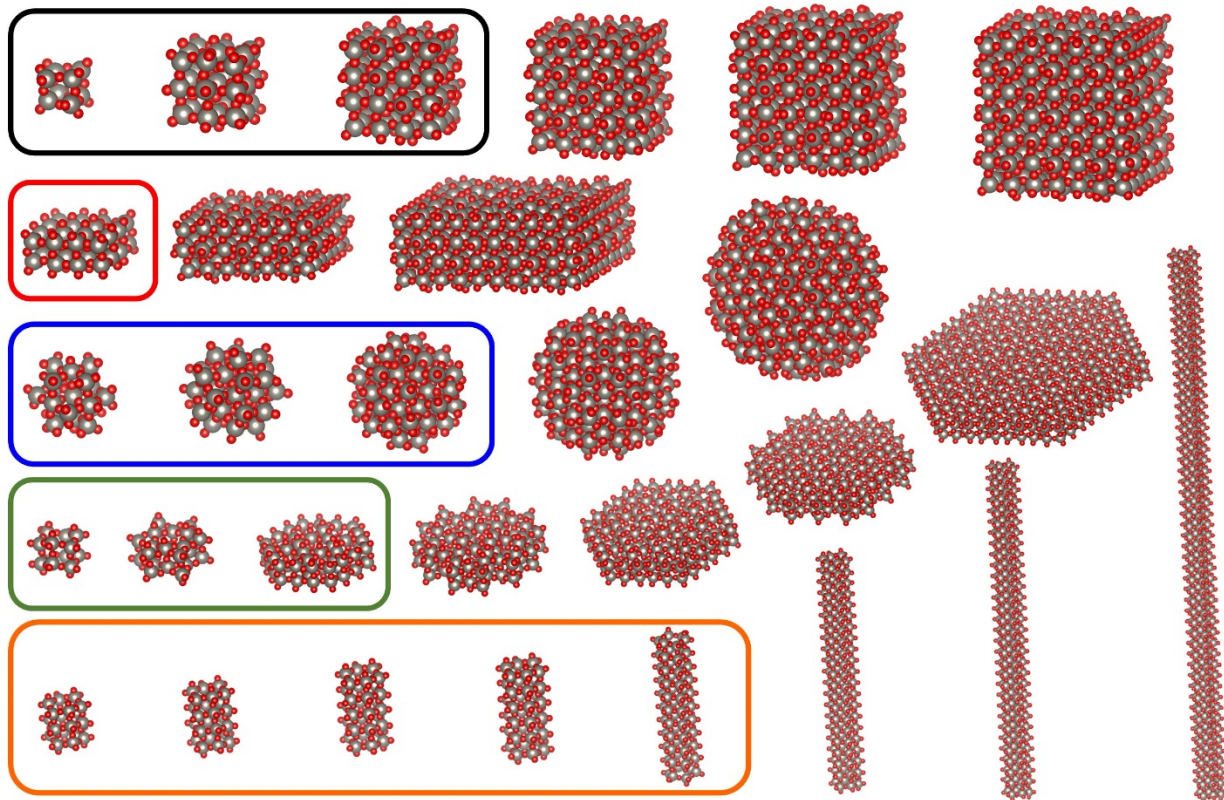


Figure 1. Perspective view of the cubic, rectangular, spherical, nanosheet and nanowire (from the top to the bottom) WO_3 nanostructures investigated in this work. The highlighted NPs are the ones used as a subset for performing the reference TD-DFT calculations.

GW/BSE calculations

The excited state calculations have been performed by solving the BSE⁶⁸ on the top of the electronic structure of the NPs calculated at the GW level. In the GW formalism the quasi-particle (QP) energies are obtained on the basis of the dynamical response to a perturbation applied to the Kohn-Sham (KS) DFT orbitals. Two different GW approaches have been employed in this work: the one-shot GW approximation (G_0W_0) and the eigenvalue partially self-consistent GW (ev GW), where the self-energy (Σ) is computed by iterating both G and W ; while keeping frozen the KS

orbitals during the self-consistent cycle. In our particular case we employed the KS orbitals calculated with the Perdew-Burke-Ernzerhof (PBE) functional⁴⁰ as starting point, due to the good results provided by the $G_0W_0@PBE$ method for the estimation of the WO_3 NPs GS properties.³¹ These calculations were carried out within a full-electron numerical atomic-centered orbital (NAO) basis set, as implemented in the Fritz Haber Institute ab initio molecular simulations (FHI-AIMS) program package.⁴¹ A Tier-1 basis set with light grid has been used, which yielded to a similar quality with respect to the valence triple- ζ plus polarization Gaussian Type Orbitals (GTO) basis set.⁴² Relativistic effects have been accounted by employing the Zero-Order Random Approximation (ZORA) to the Dirac equation.^{43,44} Finally, the resolution of the BSE has been done by relying on the Tamm-Dancoff Approximation (TDA)⁴⁵ as it has been recently developed in FHI aims code.⁴⁶

The optical properties of the monoclinic bulk phase have been computed adopting a plane wave basis set, and considering the core electrons by means of the Projected Augmented Wave (PAW) method,⁴⁷ as it is implemented in the Vienna Ab initio Simulation Package (VASP) 5.4.4 package. The DFT Kohn–Sham (KS) energies have been corrected through single-shot GW calculations (G_0W_0). To get the QP gap converged within ~ 10 meV, we considered 440 bands (i.e. 312 empty bands). Afterwards, we computed the absorption spectrum by solving the BSE, including the 6 highest Valence Bands (VBs) and 6 lowest Conduction Bands (CBs) to ensure converged exciton energies within ~ 10 meV. All calculations have been carried out at the experimental geometry⁴⁸ and by computing the exchange and correlation energies with the local density approximation (LDA) of Ceperley and Alder.⁴⁹ We used an energy cutoffs equal to 500 eV and 200 eV for the plane wave basis sets and the evaluation of the polarizability matrix, respectively, and the

reciprocal space has been sampled by employing a 6x6x6 k-points grid following the Monkhorst–Pack scheme.⁵⁰

TD-DFT calculations

For the sake of coherence with the DFT functionals used as starting points in the *GW*/BSE method, the standard hybrid PBE functional (PBE0)⁵¹ with a Hartree-Fock (HF) exchange correlation (xc) fraction of 25% was used to perform the TD-DFT calculations. We used a 3-21G* basis set for the O atoms, whereas a LanL2MB type⁵² of basis was employed for the W atoms. It is important to stress that we relied on this type of basis set in view of the large number of atoms containing the largest nanostructures and more importantly, because the use of larger basis sets for both O and W atoms was not translated into a gain of accuracy in the description of the absorption properties of the NPs, as showed in Figure S1 in Supporting Information. Similarly to the resolution of the BSE, we relied on the TDA to estimate the excited state properties of the WO₃ nanostructures since the discrepancies in energies with respect to their TD equivalents were negligible (< 0.1 eV), as is apparent in Table S1 in Supporting Information. For the evaluation of the emission properties of the WO₃ NP we first optimized the GS geometries, prior to the relaxation of the excited state (ES) of interest. We used an implicit water solvent environment to mimic the experimental conditions of the optical measurements, which was accounted for by means of the Conduction Polarizable Continuum Model (CPCM).⁵³ All this set of calculations were performed within the Gaussian 09 package.⁵⁴

sTD-DFT calculations

The DFT GS properties estimated with the Gaussian code were used as a basis to compute the excited states by following the sTD-DFT formalism, as it is implemented in the grimme-lab/stda

set of tools.^{37,38} Also in this case, TDA was employed in the simplified scheme (sTDA) in view of the similar results obtained when compared with the sTD-DFT calculated values (see Table S1 in Supporting Information). Finally, all simulated spectra were estimated by convoluting all computed vertical transitions with Gaussian function of half-width at full-length of $\sigma=0.09$ eV. Note that such a small σ value is required due to the large number of states contributing to the spectra and was set as a compromise between the magnitudes needed to fairly reproduce the experimental spectra for both small and large nanostructures.

Calculation of the exciton lifetimes

The exciton radiative lifetimes of our WO₃ NPs have been evaluated by resorting to the Fermi's golden rule implemented for a *0D* system within the excited state properties calculated at the sTDA level, as it is explained with more detail in ref.⁵⁵ Within this method, due to the absence of a crystalline momentum in a *0D* system, each excited state (in our case the lowest energy one) exhibiting a non-zero transition dipole possess an exciton recombination radiative rate at zero temperature, also known as the Einstein coefficient (A_{10}). Then the exciton lifetime is evaluated as the inverse of this coefficient by employing the formula:

$$\tau_{(1\rightarrow 0)} = \frac{1}{A_{10}} = \frac{2\pi\epsilon_0 m_e c^3}{n\omega^2 e^2 f_{(1\rightarrow 0)}} \quad (1)$$

Where ϵ_0 , m_e , c and e are the familiar fundamental constants, n is the reflective index of the medium which was set to 1.333, ω are the excitation energies, and $f_{(1\rightarrow 0)}$ the oscillator strengths. Hence, for a finite temperature, the effective radiative recombination rates are estimated by taking a thermal average only over different exciton states (s) by employing Boltzmann distributions as follows:

$$\langle A_{10}(T) \rangle_{eff} = \frac{ne^2}{2\pi\epsilon_0 m_e c^3} \frac{\sum_S f_{(1 \rightarrow 0)_S} \omega_s^2 e^{-\omega_s^2/k_b T}}{\sum_S e^{-\omega_s^2/k_b T}} \quad (2)$$

3. Results and discussion

Benchmark on a sub-set of representative NPs

Since the excited state properties of the nanoscale particles can be only tackled by using the simplified Grimme's sTDA approach, here we benchmark this method against reference BSE and TD-DFT calculations, as well as against the available experimental data, considering the smallest cubic $(\text{WO}_3)_8$ NP as our reference model.

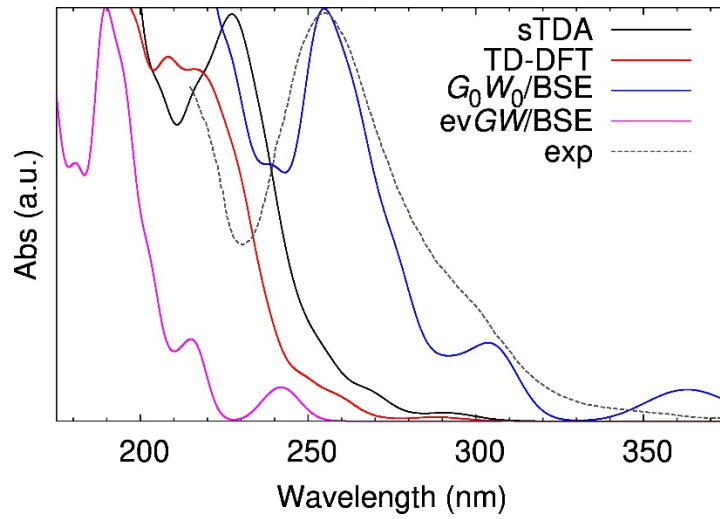


Figure 2. Simulated absorption spectra for the cubic $(\text{WO}_3)_8$ NP, as estimated with the sTDA (black), the TD-DFT (red), G_0W_0 /BSE (blue), and $evGW$ /BSE (magenta color) approaches. Note that the experimental spectrum of the WO_3 QD from ref. 16 has also been represented with dotted grey lines.

The calculated absorption spectra are plotted in Figure 2, where we compare them with the absorption features displayed by the smallest WO_3 QD reported in the literature (1.3 nm), for which, however, the morphology is not known.¹⁶ As is apparent, the agreement between the GW/BSE spectrum and the experimental one is remarkable, both in terms of energies and absorption profile. In this case, the use of partially self-consistent GW energies for the GS did not translate into a gain of accuracy, being the $evGW/BSE$ spectrum largely blue-shifted (~ 1.64 eV) with respect to the reference data. However, the intensity of the lowest energy states of the GW/BSE spectrum (~ 360 nm for G_0W_0 and ~ 240 nm for $evGW$) is clearly overestimated if we compare with the experiments. Indeed, this feature is not observed in the sTDA and TD-DFT spectra which, in turn, exhibit absorption bands which are 0.85 and 0.57 eV blue-shifted, respectively, with respect to the experimental data. Nonetheless, this can be easily corrected by employing DFT functional with larger amounts of HF xc fraction and more importantly, the overall shape of the experimental spectrum is quite well reproduced, especially in the case of the sTDA approach. It is noteworthy to mention that the discrepancies found between the theoretical and experimental absorption energies may be also related to the choice of the model, since here we are comparing the spectrum of this NP with one among the experimental ones for which no details about the QD morphology were provided.

In a second step, we have selected several representative nanostructures, comprising the small and medium size for each NPs' family, to evaluate the performance of the sTDA approach with respect to full TDA results. The first excited state energies (E_{S1}) computed by using these two different approaches are displayed in Figure 3. Note that, at this stage, we have chosen the lowest-energy transition, E_{S1} , as representative of the overall absorption properties, without any consideration if this state is dark or bright. Regardless of the NPs' family, the E_{S1} values calculated with sTDA

results overestimated for about 0.1-0.3 eV with respect to the ones computed with TDA. However, since this deviation increases monotonically with the NP size, the E_{S1} quantities estimated by both methods follow an almost linear relation. Similar sTDA vs TDA trends were found for the E_{S1} values calculated in the gas phase (see Table S2). Thus, one can employ the correlations found in Figure 3 to correct the sTDA exciton energies.

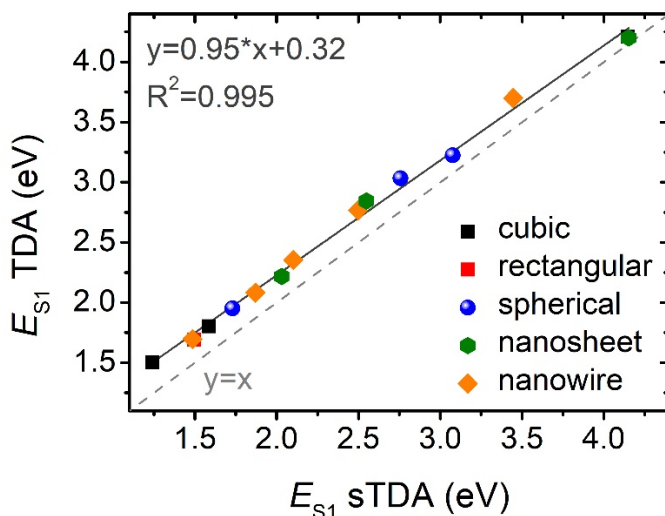


Figure 3. Correlation of the E_{S1} energies calculated at the sTDA vs TDA levels of theory for the subset of NPs highlighted in Figure 1.

Evolution of the absorption and excitonic properties with size and morphology

Having validated the accuracy of the sTDA method to reproduce the excited states of the WO_3 NPs, we can move now to investigate the influence of the NP size and morphology on their optical properties. To this aim, we have considered all the experimental absorption spectra of WO_3 nanostructures reported in the literature to employ them as a reference for validating our sTDA calculations. The results of the sTDA computed spectra for all NPs belonging to the cubic,

rectangular, and spherical families (the 3D nanomaterials), and their comparison with the reference experimental data are presented in Figure 4.

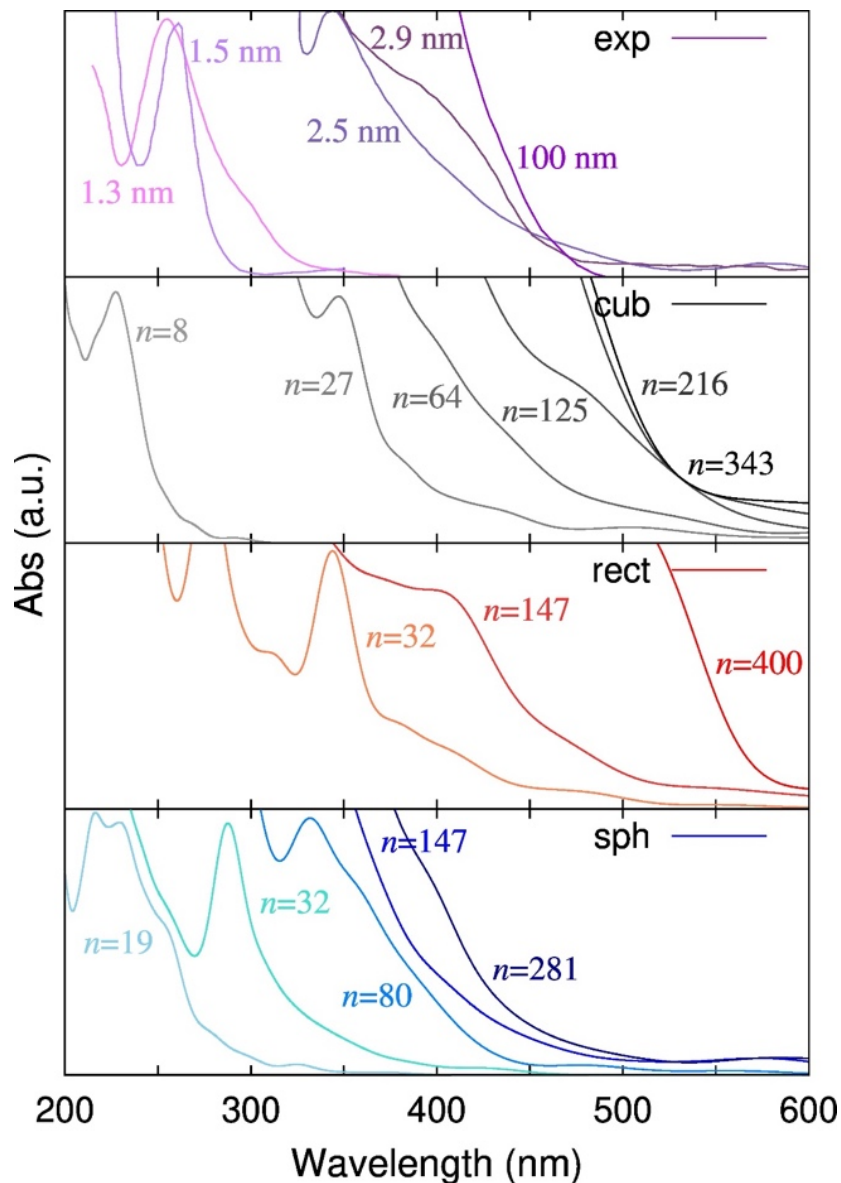


Figure 4. Simulated absorption spectra for all set of cubic (black), rectangular (red) and spherical (blue) NPs depicted in Figure 1 as calculated by sTDA (from the top to the bottom). The experimental available spectra (purple) are plotted in the top panel. Note that the color darkness used to represent each NP family increases with the size of the nanostructure, and that the NP

diameters and number of units for each experimental and theoretical spectrum, respectively, are indicated inset.

Starting with the cubic NPs, we can observe that the agreement between the computed and the experimental spectra is remarkable: the shape and energy of our $n=8$, $n=27$, and $n=125$ $(\text{WO}_3)_n$ cubic models fit pretty well with the absorption spectra of the 1.3-1.5,^{15,16} 2.5,²⁶ and 2.9 nm⁵⁶ diameter QDs, respectively. Note that the size of the experimental QDs is larger with respect to the models employed here to reproduce their absorption spectra. For instance, the computed spectra for the smallest cubic NP model, having a lateral size about 0.5 nm, reproduce quite well the experimental one obtained from 1.3-1.5 nm diameter QDs. Despite of this, the evolution of the absorption features with the NP size observed experimentally is nicely captured by our models, thus showing an excellent qualitative agreement with the experimental data. In this regard, the smallest NP presents a sharp lowest energy absorption band centered at 250 nm composed of a discrete number of states, with a considerable number of dark charge transfer (CT) states in the VIS region. For the medium size NPs, the lowest absorption band corresponds to a broad shoulder around 360 nm, which is located between the low energy CT states and the higher energy continuous band. The core-to-edge CT nature of the lowest energy states of these NPs has been confirmed by analyzing the Natural Transition Orbitals (NTOs)⁵⁷ and the TheoDORE CT density-matrix analysis⁵⁸ of these states (see Figure 5 and Table S3 in Supporting Information). These data evidenced that these CT states are originated by the presence of unoccupied states located around the W atoms at the surface.

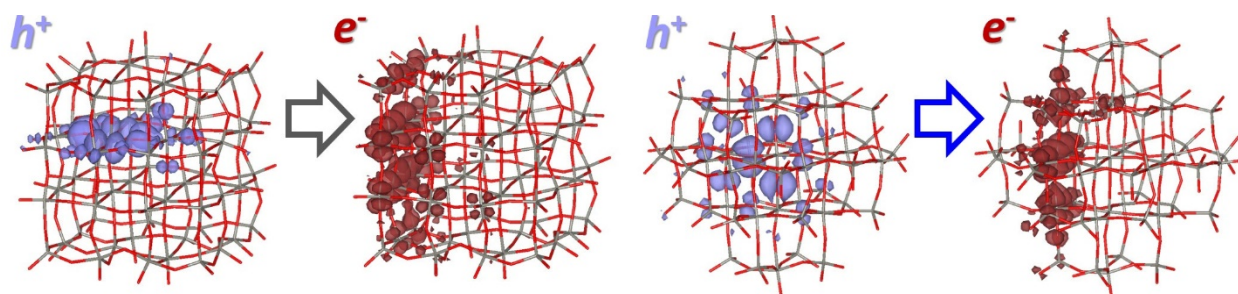


Figure 5. NTOs for lowest energy state of the cubic $(\text{WO}_3)_{64}$ (left) and spherical $(\text{WO}_3)_{57}$ (right part) NPs. Horizontal arrows are used to represent the hole to electron excitations. The isovalue used to plot the isodensity was set to 0.02 a.u. The rest of the three lowest energy states for both nanostructures are presented in Figures S2 and S3.

Finally, the larger nanostructures display an almost continuum absorption, similarly to what observed experimentally for the bulk phase.⁵⁹ For this reason, the absorption threshold obtained by Tauc plot band edge measurements is commonly employed to estimate the band gap of the bulk-like WO_3 materials.⁶⁰ Very importantly, the band edges of the larger NPs start to converge with $n=216$ (2 nm of lateral dimension) and present an absorption threshold about 550 nm, which is clearly underestimating the gap energies measured for the monoclinic bulk phase (475 nm)¹⁷ by about 0.4 eV. Concerning the rectangular NP family, the smallest nanostructures ($n=32$ and $n=147$) display similar spectral shapes with respect to the cubic NPs of the same size ($n=27$ and $n=64$). Furthermore, the largest system ($n=400$) displays an absorption band offset (570 nm) very close to the one of cubic family, thus underestimating the experimental bulk gap values to a similar extent. In spite of this, the calculated absorption edge energies for these NP families (cubic and rectangular) were in fair agreement with the ones reported for hydrated WO_3 nanoplates (550 nm).^{27,61} For the spherical NPs, these systems showed a similar evolution of the spectra with the size as the cubic family, with the $n=19$ and $n=32$, $n=80$, $n=147$ and $n=281$ reproducing the

experimental absorption features for the small, medium and large QDs, respectively. However, in this case the absorption thresholds achieved by larger nanostructures converged with respect to their size to an energy of 455 nm, thus showing a good match with the experimental values with a small over- and under-estimation (0.1 eV) of the bulk¹⁷ and microsphere NP²⁷ gaps, respectively. More importantly, our calculations fairly reproduced the band gap expansion of about 0.4 eV observed experimentally when moving from cubic-like to spherical NPs.²⁷ In a similar way, the *GW*/BSE simulated spectrum of the monoclinic bulk phase showed an absorption threshold around 400 nm (see Figure S4 in Supporting Information), which yielded to an overestimation of the experimental optical gap by 0.5 eV. Similar overestimation of the electronic gaps computed at the *GW* level have reported previously for the bulk phase.¹⁸ On overall, it appears that standard hybrid functional can quite accurately reproduce the bulk-like absorption edge energies of the spherical NPs within a precision even better than high-accurate perturbative methods, whereas for the cubic and rectangular morphologies larger amounts of HF exchange may be necessary.

Moving to the lower-dimensional NPs (nanosheets and nanowires), their absorption features are quite different with respect to the previous NPs due to their 2D- and 1D-like nature and their distinct bulk phase (monoclinic vs hexagonal). In the case of the nanosheets, their lowest energy absorption characteristics depend on their particular surface termination (see Figure 1): the hexagonal-like termination NPs ($n=12, 60, 144,$ and 420) exhibit a sharp absorption peak, whereas the star-like termination NPs ($n=24, 84,$ and 180) display a broad shoulder peak located between the CT and the continuous absorption band (see Figure S5). In both cases the energies of these absorption bands are not largely affected by the size of the NP, being located at 350 nm for the hexagonal-like, and at 380 nm for the star-like nanosheet particles. This could be ascribed to a high localization of the excitations on the NP core, whose size already converges for medium

systems (see Figure S6). Finally, the absorption of the nanowire particles in their lowest energy region is dominated by a broad band, whose energies span from 280 nm for the $n=18$ NP to 525 nm for the $n=126$ system (see Figure S7). Notably, the absorption characteristics of this NP family are well-converged for a size of $n=126$ (7.6 nm of length). These results confirm the marked dependence of the morphology in the absorption properties of WO_3 nanostructures and the possibility of targeting the absorption at different wavelengths of the UV-Vis region by controlling the size of the synthesized NP.

With the aim of getting a deeper knowledge of the excitonic behavior of our WO_3 NPs we have estimated their exciton lifetimes by following the procedure described in the last part of the Methodological section. Note that, in view of the impossibility of analyzing the NPs in their excited state relaxed geometries due to the prohibitive computational overhead needed for these calculations, we resort to the lifetimes calculated in their GS geometries, assuming that the emission is taking place via radiative recombination, as it has been established in previous theoretical works.⁶² For the cubic and rectangular NPs the computed lifetimes lie within a range of few to some dozens of μs (see Figures S8 and S9). Contrary to intuition, the largest NPs of the cubic family are the one displaying the highest lifetime, due to a marked core-to-edge CT character at the nanoscale resulting in low oscillator strength coefficients. Nonetheless, for both cubic and rectangular largest structures these lifetimes are considerably decreased when increasing the temperature, thus indicating a large destabilization of the excitons due to thermal effects for these NPs. In a similar way, spherical NPs displayed lifetimes within the same range of values, with the exception of the largest NP ($n=281$), whose estimated lifetime amounted to 0.5 μs (see Figure S10). This difference in the lifetime magnitude when compared with the smaller NPs of the same family can be traced back to the change of HOMO nature (delocalized on the surface/core for the

small/large NPs) observed when increasing the NP diameter up to 6.9 nm,³² thus yielding to a significant reduction of the CT character. Regarding the hexagonal nanostructures, their lifetimes were found slightly lower in some NPs which showed lifetimes in the order of the 0.1 μ s scale (see Figures S11 and S12). Among them, the one exhibiting the shortest lifetimes (0.01 μ s) corresponds to the largest WO₃ NP considered in our study (n=420 units), indicating that the calculated lifetimes may not be converged with respect to the NP size and confirming the general trend of the lifetime decrease when moving to bulk-like structures. Notably, the range of exciton lifetimes estimated in our work was found quite similar with respect to the one calculated for TiO₂ NPs by relying on a similar approach (0.05-50 μ s), but with the excited states computed at the full TDA level.⁶² By comparing our calculated values (in the μ s scale) with the experimental lifetimes of the WO₃ thin films obtained by time-resolved PL spectroscopy, amounting to few ns and displaying a much more pronounced bulk-like behaviour,²³ we can individuate a mayor role played by surface termination effects in the emission properties, which may become dominant when increasing the surface-to-volume ratio up to a certain extent. This conclusion goes in line with the intensity enhancement and red-shift of the emission peaks observed when moving from thin films to needle-like nanostructures, being the proportion of surface atoms much higher in the latter case.²⁴ Before closing this section, it is important to highlight that the best reference to compare our calculated exciton lifetimes will be the values measured experimentally for WO₃ QDs; which, as the best of our knowledge, are not currently available in the literature.

Unraveling the emission properties of WO₃ NPs

In view of the good capability of cubic (WO₃)₈ NP to capture the absorption properties of the 1.3-1.5 nm QDs,^{15,16} we have employed this model to investigate the emission properties displayed by these nanomaterials. It is noteworthy to mention that we stucked to the smallest NP model since

the relaxation of the bright ES of larger structures becomes computationally prohibitive in view of the huge number of states involved in this process (> 200 states). Figure 6-a represents the simulated absorption spectrum of the cubic $(\text{WO}_3)_8$ NP, which is compared with the experimental reference placed on the top panel of the figure. Clearly, the main transitions which are conforming the lowest energy absorption band from the experiments correspond to the states S_{22} and S_{57} (the ones depicted with blue and purple arrows, respectively), which are located at 273 and 254 nm, respectively. Assuming that these states are the ones which are populated upon photoexcitation, we have thus proceeded to their geometrical relaxation. It is important to highlight at this stage that due to the large number of states involved in the ES relaxation, many crossings of states are expected to take place during this process, which makes it impossible to get a clear correlation between the states of departure and the ones of the relaxed geometries. In this viewpoint, we have focused our analysis on the structural properties and the nature of the emitting states in the ES geometries. Upon ES relaxation, both S_{22} and S_{57} display similar geometries (see Table S4 and Figure S13 in Supporting Information), and more importantly, both ES geometries present emission lines (Table S5 in Supporting Information), which appear at 357 nm in both cases corresponding to emission from the S_9 state (see Figure 6-b). This finding is in perfect agreement with the experimental evidences, since the position of the emission peak displayed by WO_3 QDs was found independent of the excitation wavelength.¹⁶ It is important to highlight that the lowest energy states below S_9 were not considered responsible of the emission in view of the experimental PL evidences, since both its exciton wavelength independence and the high reported PL quantum yields (13.5%) pointed to a radiative recombination through a strong luminescent bright channel.¹⁶ In a further step, we have relaxed the S_9 state starting from the S_{22} and S_{57} geometries to check if the emission from this state ($S_9(S_{20})$ and $S_9(S_{57})$ in the following) is close to the one displayed from

these S_{22} and S_{57} relaxed structures. Interestingly, despite their different structural properties, $S_9(S_{22})$ and $S_9(S_{57})$ geometries present their emitting states at 370 and 363 nm, respectively. As a result, we can conclude that all ES geometries display emission lines with wavelengths in the range of 360-370 nm, which is in semi-quantitative agreement (ca. 0.3-0.4 eV) with the emission peaks of the WO_3 QDs observed at 400 nm.¹⁶ With the objective of clarifying the origin of the Stoke shifts experimented by WO_3 QDs, we have evaluated the modification of the GS structural parameters upon the relaxation of the ESs, namely their bond lengths, angles, and dihedrals (see Table S4 and Figure S13 in Supporting Information). As a matter of fact, the most prominent geometrical modifications with respect to the GS geometries for both S_{22} and S_{57} states involve the shortening of one of the W-O bonds in the NP core, which entails an elongation of the neighboring W-O surface bond (see Figure S13). This bonds deformation comes from the CT character of the emitting states from the O surface states to the core (see Figure S14). Since the bright states responsible for the absorption start to localize on the NP core when increasing its size (see Figure S15), the impact of this local deformation of the surface bonds in the emission properties of larger NP is expected to be lower, as it has been confirmed by the fact that the Stoke shifts of WO_3 QDs halves by increasing 1 nm their diameter, as discussed in the introduction.^{15,16,26} These findings suggest that the excitonic behavior of WO_3 QDs can be enhanced by reducing their size and increasing the number of surface bonds, for instance, by using spherical-like morphologies.

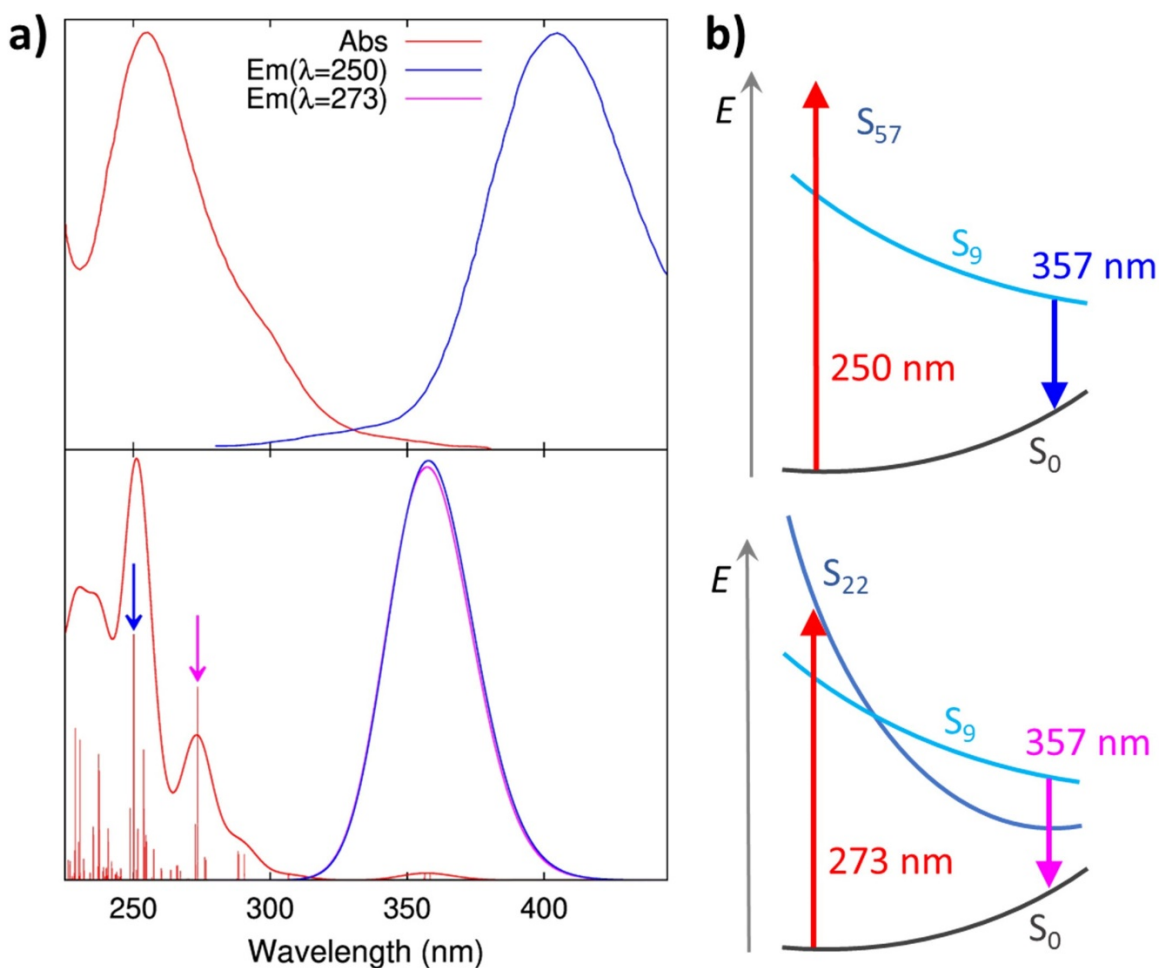


Figure 6. a) Absorption and emission spectra for the QDs reported in ref. 16 (top); and for the cubic $(\text{WO}_3)_8$ NP estimated with TD-DFT by following the relaxation of brightest states in the GS geometry (S_{57} (blue) and S_{22} (pink arrows)), and considering that the states responsible of the emission lines are the lowest energy bright states in the ES geometries (see the computed absorption spectra at the S_{57} and S_{22} geometries with dashed lines); b) energetic scheme of the ES relaxation pathways followed by the S_{57} and S_{22} and their emission in their correspondent minima.

4. Conclusions and perspectives

Herein we have reported an unprecedented theoretical study of the optoelectronic properties of WO_3 nanostructures, mainly focusing on their absorption and emission spectra, and their exciton

lifetimes. Firstly, we have validated the simplified Grimme's method, sTDA, used here to evaluate the optical properties of realistic nanoscale particles, by benchmarking the results against MBPT, full TD-DFT methods and experiments, when available, for small and medium size NPs. Interestingly, we have found that for this range of sizes, sTDA can provide estimations of the absorption energies upon correction of the systematic underestimation of energies with respect to the TD-DFT values, within the same precision as TD-DFT; whereas for the reproduction of the overall shape of the simulated spectra, this method performed even better than TD-DFT or MBPT approaches. Afterwards, we have investigated the evolution of the absorption characteristics with the size and morphology of the NP. Interestingly, our models have been able to reproduce the characteristic absorption features of the small, medium, and large WO₃ nanostructures reported experimentally, whereas the energies of the size-converged spectra were diverging as a function of the NP morphology. In a final step, we have analyzed the emission properties of WO₃ QDs by evaluating the relaxation of the lowest energy bright states of the reference cubic NP, and by estimating the exciton lifetimes for all series of NPs. These results demonstrated that all ES geometries are characterized by a local distortion of the surface W-O bonds and by emission lines centered at 360-370 nm, which are in nice agreement with the ones observed experimentally at 400 nm. On the same vein, the different order of magnitude in the calculated exciton lifetimes (μ s scale) in our NPs with respect the experimental values measured for thin films (few ns) demonstrated that in WO₃ QDs the emission lines are mainly dominated by surface termination effects, thus pointing to surface treatment methods as the most efficient strategy to monitor the emission properties of these materials.

We show here that by setting up reliable theoretical and structural models one can investigate the photophysical properties of WO₃ nanostructures and draw useful structure-properties relationships

to tune absorption and emission properties of WO_3 NPs. With this work, we aim to encourage the opto-electronics community to put more research effort in clarifying the photophysics of WO_3 QDs, for instance, by evaluating their exciton dynamics via Transient Absorption Spectra (TAS) or time-resolved PL spectroscopy measurements. The combination of these experimental outcomes and our theoretical models can pave the way to a more efficient utilization of WO_3 nanomaterials for opto-electronic purposes what, combined with their good biocompatibility and high chemical and structural stability, can bring them to the commercial exploitation in many conditions and environments which are barely accessible for traditional QDs.

ASSOCIATED CONTENT

Supporting Information

The Supporting Information is available free of charge on the ACS Publications website. Benchmarking of the basis sets, simplified vs full TD-DFT and TDA approaches, and gas phase vs water solvent environments; NTOs lowest energy states cubic $(\text{WO}_3)_{64}$ and spherical $(\text{WO}_3)_{57}$ NPs and corresponding CT transition density matrix analysis; simulated absorption spectra for the bulk, nanosheet and nanowire set of NPs; MOs shapes for the main contributions to the lowest energy bright state of the nanosheet $(\text{WO}_3)_{60}$ particle; temperature-dependency of the exciton lifetimes for the cubic, rectangular, spherical, nanosheet and nanowire NP families; geometrical and excited state properties of cubic $(\text{WO}_3)_8$ NP in its GS and ES structures; NTOs of the emitting states of the cubic $(\text{WO}_3)_8$ NP, and of the absorbing states of the cubic $(\text{WO}_3)_8$ and $(\text{WO}_3)_{27}$ NPs.

AUTHOR INFORMATION

Corresponding Authors

Valentin Diez-Cabanes- *Université de Lorraine & CNRS, Laboratoire de Physique et Chimie Théoriques (LPCT), F-54000, Nancy, France.* ORCID: <https://orcid.org/0000-0002-6234-2749>.

Email: valentin.diez-cabanes@univ-lorraine.fr

Mariachiara Pastore- *Université de Lorraine & CNRS, Laboratoire de Physique et Chimie Théoriques (LPCT), F-54000, Nancy, France.* ORCID: <https://orcid.org/0000-0003-4793-1964>.

Email: mariachiara.pastore@univ-lorraine.fr

Author

Alekos Segalina- *Université de Lorraine & CNRS, Laboratoire de Physique et Chimie Théoriques (LPCT), F-54000, Nancy, France*

Department of Chemistry, Korea Advanced Institute of Science and Technology (KAIST), 291 Daehak-ro, Yuseong-gu, Daejeon, 34141 Republic of Korea

Notes

The authors declare no competing financial interest.

ACKNOWLEDGMENT

V.D.-C. and A. S. are grateful to the COMETE (COncEption in silico de Matériaux pour l'Environnement et l'Energie) project. V.D.-C. also thanks the “Fire Light” (“Photo-bio-active molecules and nanoparticles”) project. Both grants are co-funded by the European Union under the program FEDER-FSE Lorraine et Massif des Vosges 2014-2020. Computational resources were provided by the mésocentre EXPLOR of Université de Lorraine (Project 2018CPMXX0602), and by the LPCT local clusters.

REFERENCES

- (1) Quan, H.; Gao, Y.; Wang, W. Tungsten Oxide-Based Visible Light-Driven Photocatalysts: Crystal and Electronic Structures and Strategies for Photocatalytic Efficiency Enhancement. *Inorg. Chem. Front.* **2020**, *7*, 817–838.
- (2) Niklasson, G. A.; Granqvist, C. G. Electrochromics for Smart Windows: Thin Films of Tungsten Oxide and Nickel Oxide, and Devices Based on These. *J. Mater. Chem.* **2007**, *17*, 127–156.
- (3) Zhou, Z.; Kong, B.; Yu, C.; Shi, X.; Wang, M.; Liu, W.; Sun, Y.; Zhang, Y.; Yang, H.; Yang, S. Tungsten Oxide Nanorods: An Efficient Nanoplatform for Tumor CT Imaging and Photothermal Therapy. *Sci. Rep.* **2014**, *4*, 1–10.
- (4) Bertuna, A.; Comini, E.; Kaur, N.; Poli, N.; Zappa, D.; Sberveglieri, V.; Sberveglieri, G. Nanostructures of Tungsten Trioxide, Nickel Oxide and Niobium Oxide for Chemical Sensing Applications. *Procedia Eng.* **2015**, *120*, 803–806.
- (5) Yao, Y.; Sang, D.; Zou, L.; Wang, Q.; Liu, C. A Review on the Properties and Applications of WO₃ Nanostructure-based Optical and Electronic Devices. *Nanomaterials* **2021**, *11*, 2136.
- (6) Huang, Z. F.; Song, J.; Pan, L.; Zhang, X.; Wang, L.; Zou, J. J. Tungsten Oxides for Photocatalysis, Electrochemistry, and Phototherapy. *Adv. Mater.* **2015**, *27*, 5309–5327.
- (7) Zheng, H.; Ou, J. Z.; Strano, M. S.; Kaner, R. B.; Mitchell, A.; Kalantar-Zadeh, K. Nanostructured Tungsten Oxide - Properties, Synthesis, and Applications. *Adv. Funct. Mater.* **2011**, *21*, 2175–2196.
- (8) Chen, X.; Li, C.; Grätzel, M.; Kostecki, R.; Mao, S. S. Nanomaterials for Renewable Energy Production and Storage. *Chem. Soc. Rev.* **2012**, *41*, 7909–7937.
- (9) Wang, S.; Liu, G.; Wang, L. Crystal Facet Engineering of Photoelectrodes for

- Photoelectrochemical Water Splitting. *Chem. Rev.* **2019**, *119*, 5192–5247.
- (10) Morales-García, Á.; Macià Escatllar, A.; Illas, F.; Bromley, S. T. Understanding the Interplay between Size, Morphology and Energy Gap in Photoactive TiO₂ Nanoparticles. *Nanoscale* **2019**, *11*, 9032–9041.
- (11) Hardman, R. A Toxicologic Review of Quantum Dots: Toxicity Depends on Physicochemical and Environmental Factors. *Environ. Health Perspect.* **2006**, *114*, 165–172.
- (12) Watanabe, H.; Fujikata, K.; Oaki, Y.; Imai, H. Band-Gap Expansion of Tungsten Oxide Quantum Dots Synthesized in Sub-Nano Porous Silica. *Chem. Commun.* **2013**, *49*, 8477–8479.
- (13) Tanaka, D.; Oaki, Y.; Imai, H. Enhanced Photocatalytic Activity of Quantum-Confined Tungsten Trioxide Nanoparticles in Mesoporous Silica. *Chem. Commun.* **2010**, *46*, 5286–5288.
- (14) Ling, M.; Blackman, C. S.; Palgrave, R. G.; Sotelo-Vazquez, C.; Kafizas, A.; Parkin, I. P. Correlation of Optical Properties, Electronic Structure, and Photocatalytic Activity in Nanostructured Tungsten Oxide. *Adv. Mater. Interfaces* **2017**, *4*, 3–9.
- (15) Cong, S.; Tian, Y.; Li, Q.; Zhao, Z.; Geng, F. Single-Crystalline Tungsten Oxide Quantum Dots for Fast Pseudocapacitor and Electrochromic Applications. *Adv. Mater.* **2014**, *26*, 4260–4267.
- (16) Peng, H.; Liu, P.; Lin, D.; Deng, Y.; Lei, Y.; Chen, W.; Chen, Y.; Lin, X.; Xia, X.; Liu, A. Fabrication and Multifunctional Properties of Ultrasmall Water-Soluble Tungsten Oxide Quantum Dots. *Chem. Commun.* **2016**, *52*, 9534–9537.
- (17) Gullapalli, S. K.; Vemuri, R. S.; Ramana, C. V. Structural Transformation Induced

- Changes in the Optical Properties of Nanocrystalline Tungsten Oxide Thin Films. *Appl. Phys. Lett.* **2010**, *96*, 20–23.
- (18) Johansson, M. B.; Baldissera, G.; Valyukh, I.; Persson, C.; Arwin, H.; Niklasson, G. A.; Österlund, L. Electronic and Optical Properties of Nanocrystalline WO₃ Thin Films Studied by Optical Spectroscopy and Density Functional Calculations. *J. Phys. Condens. Matter* **2013**, *25*, 205502.
- (19) Feng, M.; Pan, A. L.; Zhang, H. R.; Li, Z. A.; Liu, F.; Liu, H. W.; Shi, D. X.; Zou, B. S.; Gao, H. J. Strong Photoluminescence of Nanostructured Crystalline Tungsten Oxide Thin Films. *Appl. Phys. Lett.* **2005**, *86*, 1–3.
- (20) Johansson, M. B.; Zietz, B.; Niklasson, G. A.; Österlund, L. Optical Properties of Nanocrystalline WO₃ and WO_{3-x} Thin Films Prepared by DC Magnetron Sputtering. *J. Appl. Phys.* **2014**, *115*, 213510.
- (21) Lee, K.; Seo, W. S.; Park, J. T. Synthesis and Optical Properties of Colloidal Tungsten Oxide Nanorods. *J. Am. Chem. Soc.* **2003**, *125*, 3408–3409.
- (22) Rajagopal, S.; Nataraj, D.; Mangalaraj, D.; Djaoued, Y.; Robichaud, J.; Khyzhun, O. Y. Controlled Growth of WO₃ Nanostructures with Three Different Morphologies and Their Structural, Optical, and Photodecomposition Studies. *Nanoscale Res. Lett.* **2009**, *4*, 1335–1342.
- (23) Petruleviciene, M.; Juodkazyte, J.; Parvin, M.; Tereshchenko, A.; Ramanavicius, S.; Karpicz, R.; Samukaite-Bubniene, U.; Ramanavicius, A. Tuning the Photo-Luminescence Properties of WO₃ Layers by the Adjustment of Layer Formation Conditions. *Materials (Basel)*. **2020**, *13*, 2814.
- (24) Park, S.; Kim, H.; Jin, C.; Lee, C. Intense Ultraviolet Emission from Needle-like WO₃

- Nanostructures Synthesized by Noncatalytic Thermal Evaporation. *Nanoscale Res. Lett.* **2011**, *6*, 1–6.
- (25) Luo, J. Y.; Zhao, F. L.; Gong, L.; Chen, H. J.; Zhou, J.; Li, Z. L.; Deng, S. Z.; Xu, N. S. Ultraviolet-Visible Emission from Three-Dimensional WO₃-x Nanowire Networks. *Appl. Phys. Lett.* **2007**, *91*, 11–14.
- (26) Wang, S.; Kershaw, S. V.; Li, G.; Leung, M. K. H. The Self-Assembly Synthesis of Tungsten Oxide Quantum Dots with Enhanced Optical Properties. *J. Mater. Chem. C* **2015**, *3*, 3280–3285.
- (27) Ou, P.; Song, F.; Yang, Y.; Shao, J.; Hua, Y.; Yang, S.; Wang, H.; Luo, Y.; Liao, J. WO₃·nH₂O Crystals with Controllable Morphology/Phase and Their Optical Absorption Properties. *ACS Omega* **2022**, *7*, 8833–8839.
- (28) Bromley, S. T.; Moreira, I. S. P. R.; Neyman, K. M.; Illas, F. Approaching Nanoscale Oxides: Models and Theoretical Methods. *Chem. Soc. Rev.* **2009**, *38*, 2657–2670.
- (29) Diez-Cabanes, V.; Pastore, M. Morphological Engineering of Inorganic Semiconductor VIS-Light-Driven Nanocatalysts: Experimental and Theoretical Understandings. *J. Phys. Chem. C* **2021**, *125*, 15125–15133.
- (30) Reining, L. The GW Approximation: Content, Successes and Limitations. *Wiley Interdiscip. Rev. Comput. Mol. Sci.* **2018**, *8*, 1–26.
- (31) Diez-Cabanes, V.; Morales-Garcia, A.; Illas, F.; Pastore, M. Understanding the Structural and Electronic Properties of Photoactive Tungsten Oxide Nanoparticles from Density Functional Theory and GW Approaches. *J. Chem. Theory Comput.* **2021**, *17*, 3462–3470.
- (32) Diez-Cabanes, V.; Morales-Garcia, A.; Illas, F.; Pastore, M. Tuning the Interfacial Energetics in WO₃/WO₃ and WO₃/TiO₂ Heterojunctions by Nanostructure

- Morphological Engineering. *J. Phys. Chem. Lett.* **2021**, *2*, 11528–11533.
- (33) Adamo, C.; Jacquemin, D. The Calculations of Excited-State Properties with Time-Dependent Density Functional Theory. *Chem. Soc. Rev.* **2013**, *42*, 845–856.
- (34) Laurent, A. D.; Adamo, C.; Jacquemin, D. Dye Chemistry with Time-Dependent Density Functional Theory. *Phys. Chem. Chem. Phys.* **2014**, *16*, 14334–14356.
- (35) Blase, X.; Duchemin, I.; Jacquemin, D. The Bethe-Salpeter Equation in Chemistry: Relations with TD-DFT, Applications and Challenges. *Chem. Soc. Rev.* **2018**, *47*, 1022–1043.
- (36) Blase, X.; Duchemin, I.; Jacquemin, D.; Loos, P. F. The Bethe-Salpeter Equation Formalism: From Physics to Chemistry. *J. Phys. Chem. Lett.* **2020**, *11*, 7371–7382.
- (37) Grimme, S. A Simplified Tamm-Dancoff Density Functional Approach for the Electronic Excitation Spectra of Very Large Molecules. *J. Chem. Phys.* **2013**, *138*, 244104.
- (38) Bannwarth, C.; Grimme, S. A Simplified Time-Dependent Density Functional Theory Approach for Electronic Ultraviolet and Circular Dichroism Spectra of Very Large Molecules. *Comput. Theor. Chem.* **2014**, *1040–1041*, 45–53.
- (39) De Wergifosse, M.; Grimme, S. Perspective on Simplified Quantum Chemistry Methods for Excited States and Response Properties. *J. Phys. Chem. A* **2021**, *125*, 3841–3851.
- (40) Perdew, J. P.; Burke, K.; Ernzerhof, M. Generalized Gradient Approximation Made Simple. *Phys. Rev. Lett.* **1996**, *77*, 3865–3868.
- (41) Blum, V.; Gehrke, R.; Hanke, F.; Havu, P.; Havu, V.; Ren, X.; Reuter, K.; Scheffler, M. Ab Initio Molecular Simulations with Numeric Atom-Centered Orbitals. *Comput. Phys. Commun.* **2009**, *180*, 2175–2196.
- (42) Lamiel-Garcia, O.; Ko, K. C.; Lee, J. Y.; Bromley, S. T.; Illas, F. When Anatase

- Nanoparticles Become Bulklike: Properties of Realistic TiO₂ Nanoparticles in the 1-6 nm Size Range from All Electron Relativistic Density Functional Theory Based Calculations. *J. Chem. Theory Comput.* **2017**, *13*, 1785–1793.
- (43) Chang, C.; Pelissier, M.; Durand, P. Regular Two-Component Pauli-like Effective Hamiltonians in Dirac Theory. *Phys. Scr.* **1986**, *34*, 394–404.
- (44) Van Lenthe, E.; Baerends, E. J.; Snijders, J. G. Relativistic Regular Two-Component Hamiltonians. *J. Chem. Phys.* **1993**, *99*, 4597–4610.
- (45) S.M. Dancoff. Non-Adiabatic Meson Theory of Nuclear Forces. *Phys. Rev.* **1950**, *78*, 382–385.
- (46) Liu, C.; Kloppenburg, J.; Yao, Y.; Ren, X.; Appel, H.; Kanai, Y.; Blum, V. All-Electron Ab Initio Bethe-Salpeter Equation Approach to Neutral Excitations in Molecules with Numeric Atom-Centered Orbitals. *J. Chem. Phys.* **2020**, *152*, 044105.
- (47) Kresse, G.; Joubert, D. From Ultrasoft Pseudopotentials to the Projector Augmented-Wave Method. *Phys. Rev. B - Condens. Matter Mater. Phys.* **1999**, *59*, 1758–1775.
- (48) Loopstra, B. O.; Rietveld, H. M. Further Refinement of the Structure of WO₃. *Acta Crystallogr. Sect. B* **1969**, *25*, 1420–1421.
- (49) Ceperley, D. M.; Alder, B. J. Ground State of the Electron Gas by a Stochastic Method. *Phys. Rev. Lett.* **1980**, *45*, 566–569.
- (50) Pack, J. D.; Monkhorst, H. J. Special Points for Brillouin-Zone Integrations. *Phys. Rev. B* **1977**, *16*, 1748–1749.
- (51) Adamo, C.; Barone, V. Toward Reliable Density Functional Methods without Adjustable Parameters: The PBE0 Model. *J. Chem. Phys.* **1999**, *110*, 6158–6170.
- (52) Wadt, W. R.; Hay, P. J. Ab Initio Effective Core Potentials for Molecular Calculations.

- Potentials for Main Group Elements Na to Bi. *J. Chem. Phys.* **1985**, *82*, 284–298.
- (53) Tomasi, J.; Mennucci, B.; Cammi, R. Quantum Mechanical Continuum Solvation Models. *Chem. Rev.* **2005**, *105*, 2999–3093.
- (54) Frisch, M. J.; Trucks, G. W.; Schlegel, H. B.; Scuseria, G. E.; Robb, M. A.; Cheeseman, J. R.; Scalmani, G.; Barone, V.; Petersson, G. A.; Nakatsuji, H.; Li, X.; Caricato, M.; Marenich, A.; Bloino, J.; Janesko, B. G.; Gomperts, R.; Mennucci, B.; Hratchian, H. P.; Ortiz, J. V.; Izmaylov, A. F.; Sonnenberg, J. L.; Williams-Young, D.; Ding, F.; Lipparini, F.; Egidi, F.; Goings, J.; Peng, B.; Petrone, A.; Henderson, T.; Ranasinghe, D.; Zakrzewski, V. G.; Gao, J.; Rega, N.; Zheng, G.; Liang, W.; Hada, M.; Ehara, M.; Toyota, K.; Fukuda, R.; Hasegawa, J.; Ishida, M.; Nakajima, T.; Honda, Y.; Kitao, O.; Nakai, H.; Vreven, T.; Throssell, K.; J. A. Montgomery, J.; Peralta, J. E.; Ogliaro, F.; Bearpark, M.; Heyd, J. J.; Brothers, E.; Kudin, K. N.; Staroverov, V. N.; Keith, T.; Kobayashi, R.; Normand, J.; Raghavachari, K.; Rendell, A.; Burant, J. C.; Iyengar, S. S.; Tomasi, J.; Cossi, M.; Millam, J. M.; Klene, M.; Adamo, C.; Cammi, R.; Ochterski, J. W.; Martin, R. L.; Morokuma, K.; Farkas, O.; Foresman, J. B.; Fox, D. J. Gaussian 09, Revision A.02. **2016**, Gaussian Inc., Wallingford CT.
- (55) Chen, H. Y.; Jhalani, V. A.; Palumbo, M.; Bernardi, M. Ab Initio Calculations of Exciton Radiative Lifetimes in Bulk Crystals, Nanostructures, and Molecules. *Phys. Rev. B* **2019**, *100*, 75135.
- (56) Zhao, Y.; Fan, H.; Li, W.; Bi, L.; Wang, D.; Wu, L. Incorporation of Polyoxotungstate Complexes in Silica Spheres and in Situ Formation of Tungsten Trioxide Nanoparticles. *Langmuir* **2010**, *26*, 14894–14900.
- (57) Martin, R. L. Natural Transition Orbitals. *J. Chem. Phys.* **2003**, *118*, 4775–4777.

- (58) Plasser, F. TheoDORE: A Toolbox for a Detailed and Automated Analysis of Electronic Excited State Computations. *J. Chem. Phys.* **2020**, *152*, 084108.
- (59) Cole, B.; Marsen, B.; Miller, E.; Yan, Y.; To, B.; Jones, K.; Al-Jassim, M. Evaluation of Nitrogen Doping of Tungsten Oxide for Photoelectrochemical Water Splitting. *J. Phys. Chem. C* **2008**, *112*, 5213–5220.
- (60) Makuła, P.; Pacia, M.; Macyk, W. How To Correctly Determine the Band Gap Energy of Modified Semiconductor Photocatalysts Based on UV-Vis Spectra. *J. Phys. Chem. Lett.* **2018**, *9*, 6814–6817.
- (61) Guo, S. Q.; Zhen, M. M.; Sun, M. Q.; Zhang, X.; Zhao, Y. P.; Liu, L. Controlled Fabrication of Hierarchical $\text{WO}_3 \cdot \text{H}_2\text{O}$ Hollow Microspheres for Enhanced Visible Light Photocatalysis. *RSC Adv.* **2015**, *5*, 16376–16385.
- (62) Cho, D.; Ko, K. C.; Lamiel-García, O.; Bromley, S. T.; Lee, J. Y.; Illas, F. Effect of Size and Structure on the Ground-State and Excited-State Electronic Structure of TiO_2 Nanoparticles. *J. Chem. Theory Comput.* **2016**, *12*, 3751–3763.

TOC Graphic

